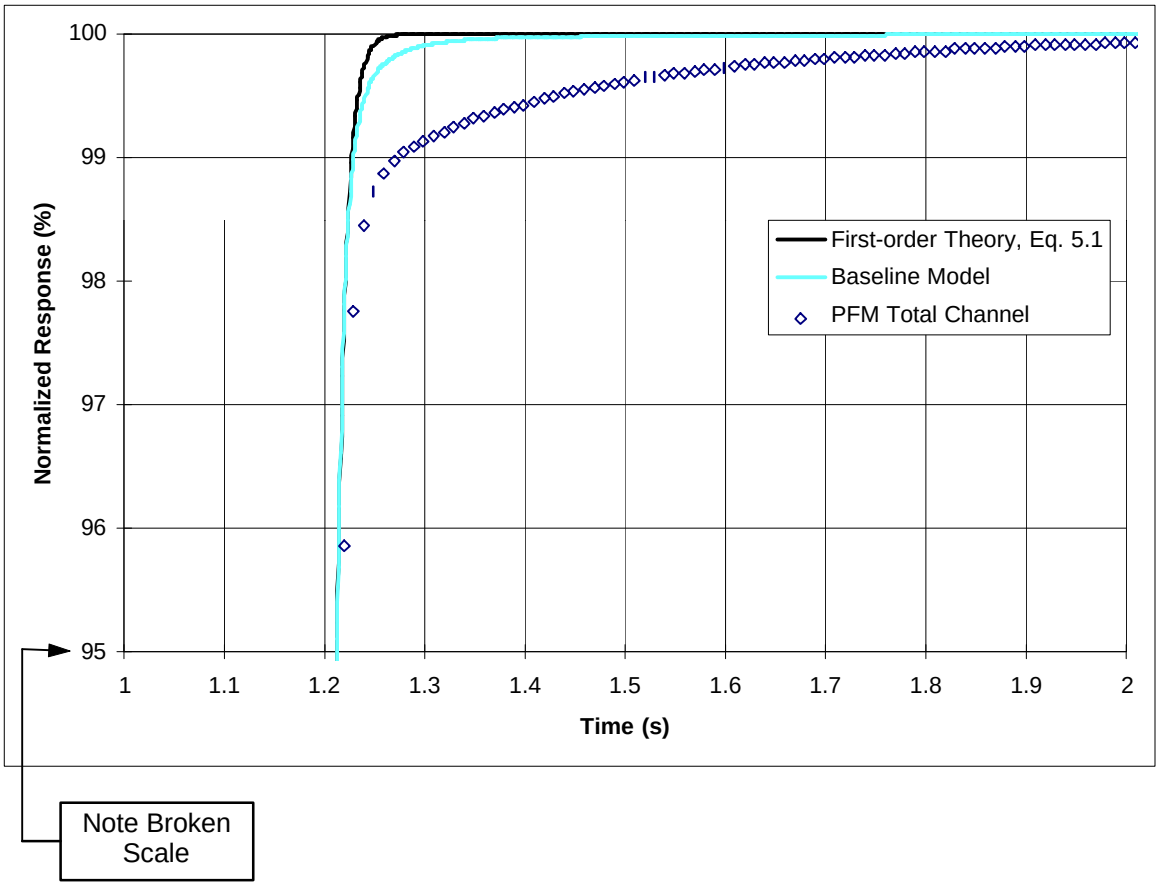

Figure 5.1 Comparison of time response functions for a theoretical first-order response, for the baseline numerical model, and for the actual PFM total channel flight sensor.

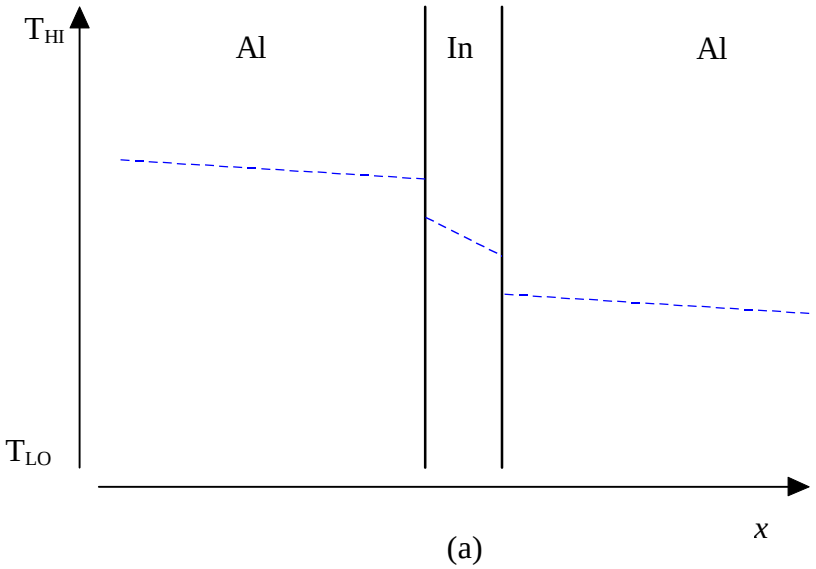

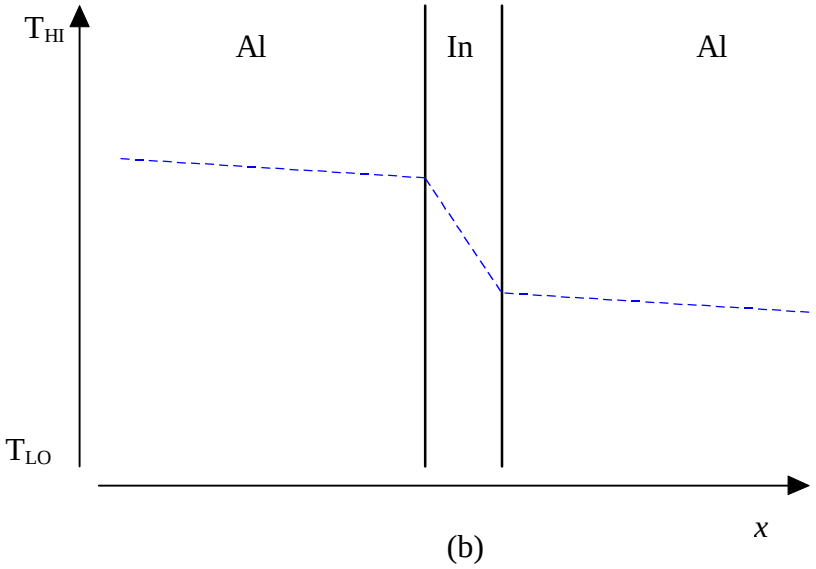

Figure 5.2 Conceptual comparison of temperature profiles for (a) actual interface resistance, and (b) modeled interface resistance.

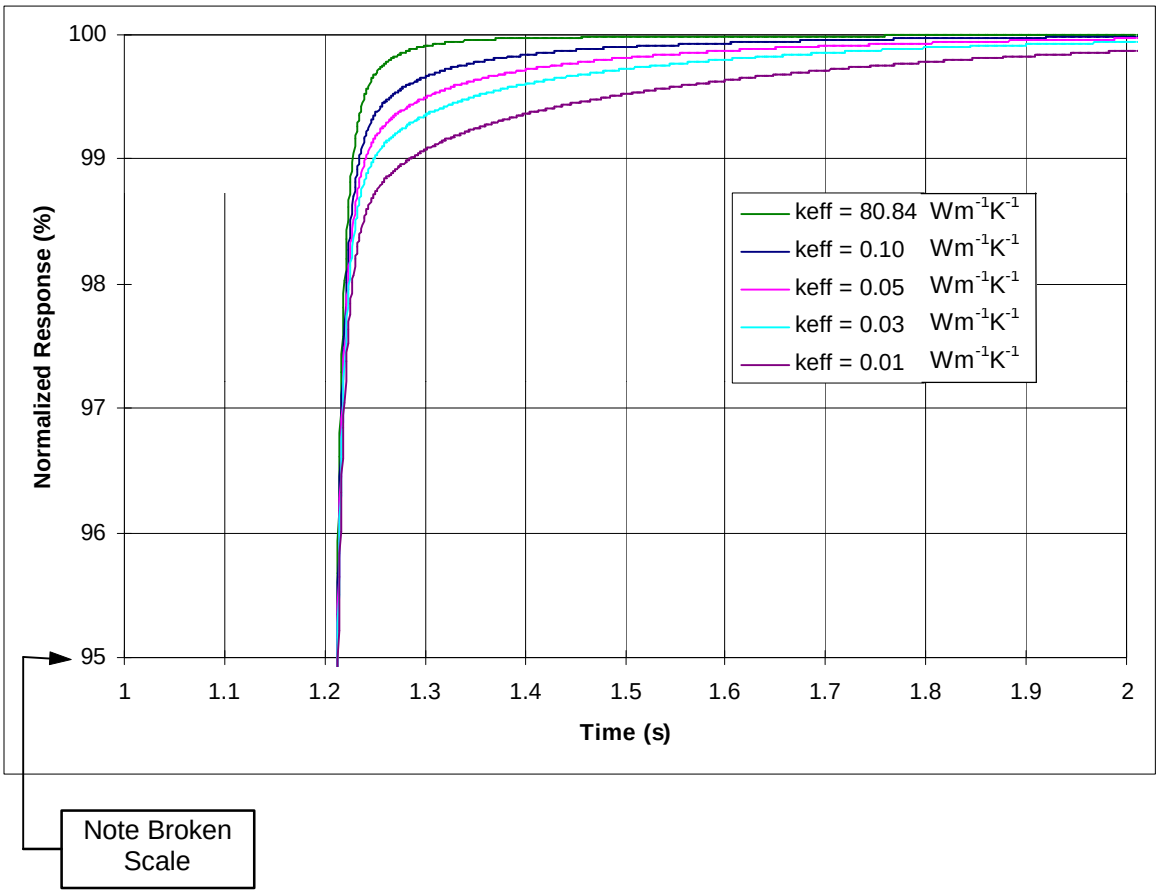

Figure 5.3 Predicted effect of varying the effective thermal conductivity of the Indium layer on the normalized time response function of the CERES detector module assembly.

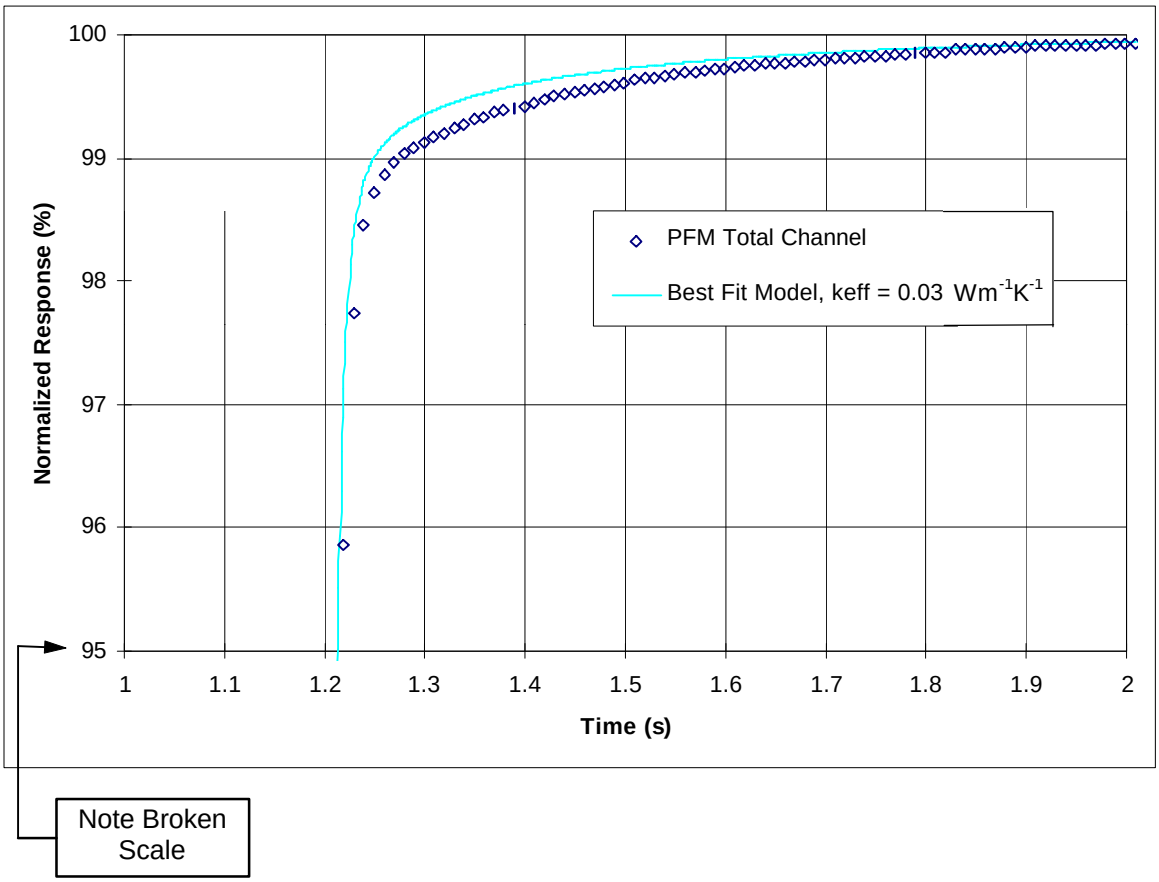

Figure 5.4 Comparison between the CERES PFM total channel sensor response functions and the “best-fit” numerical model.

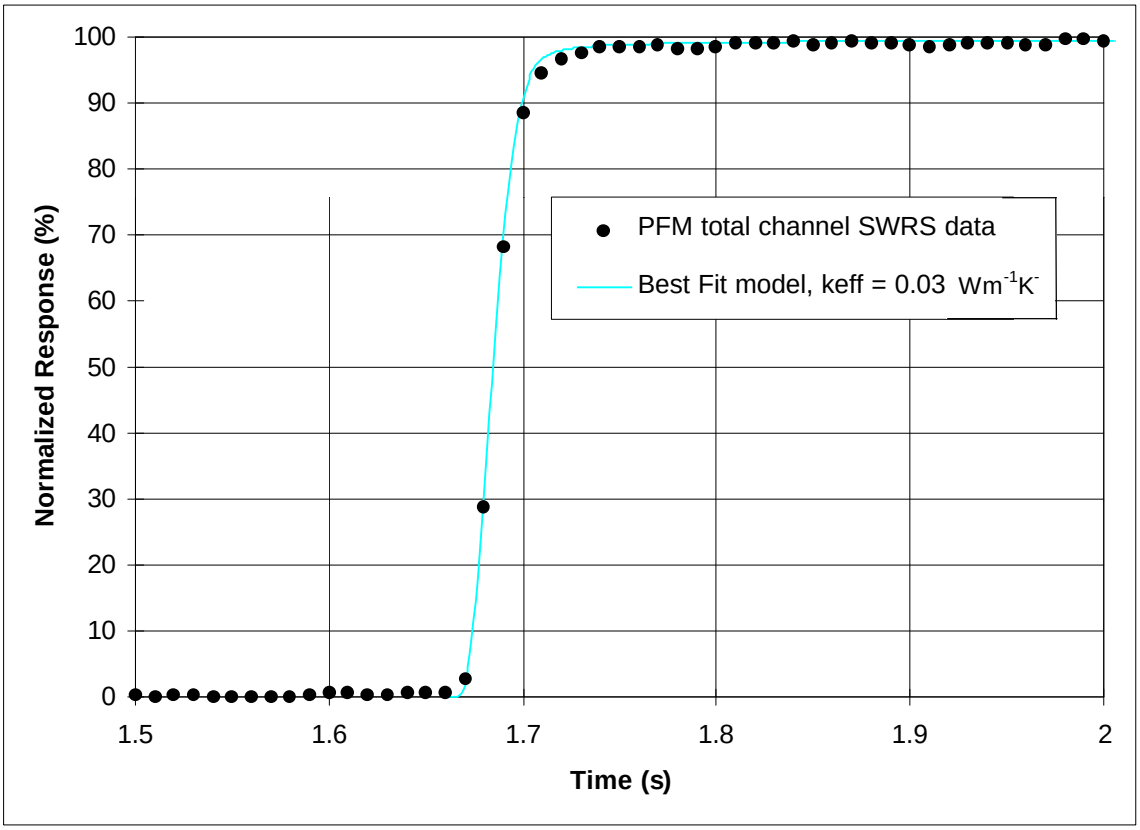

Figure 5.5 Qualitative comparison between a numerically simulated step input from the "best-fit" numerical model and chopped data from the Short Wave Reference Source (SWRS) calibration for the PFM total channel.

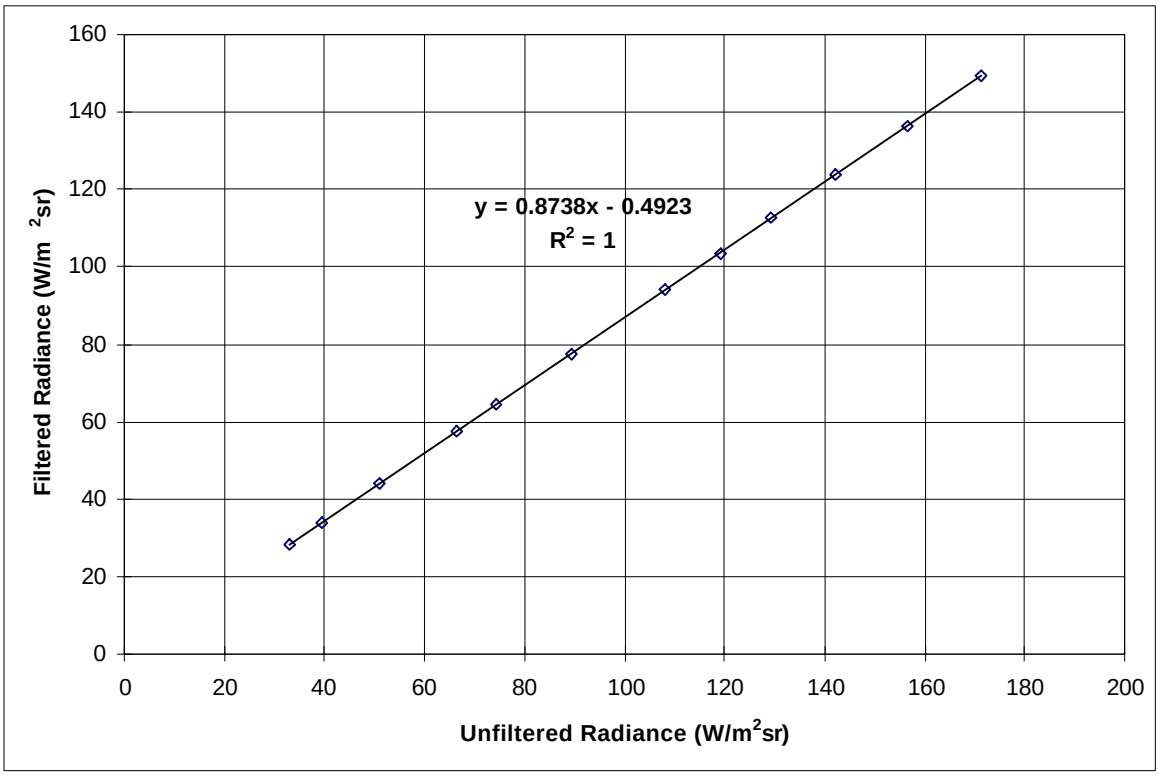

Figure 5.6 Relationship between the longwave filtered and unfiltered radiances from the radiometric ground calibration for the PFM total channel.

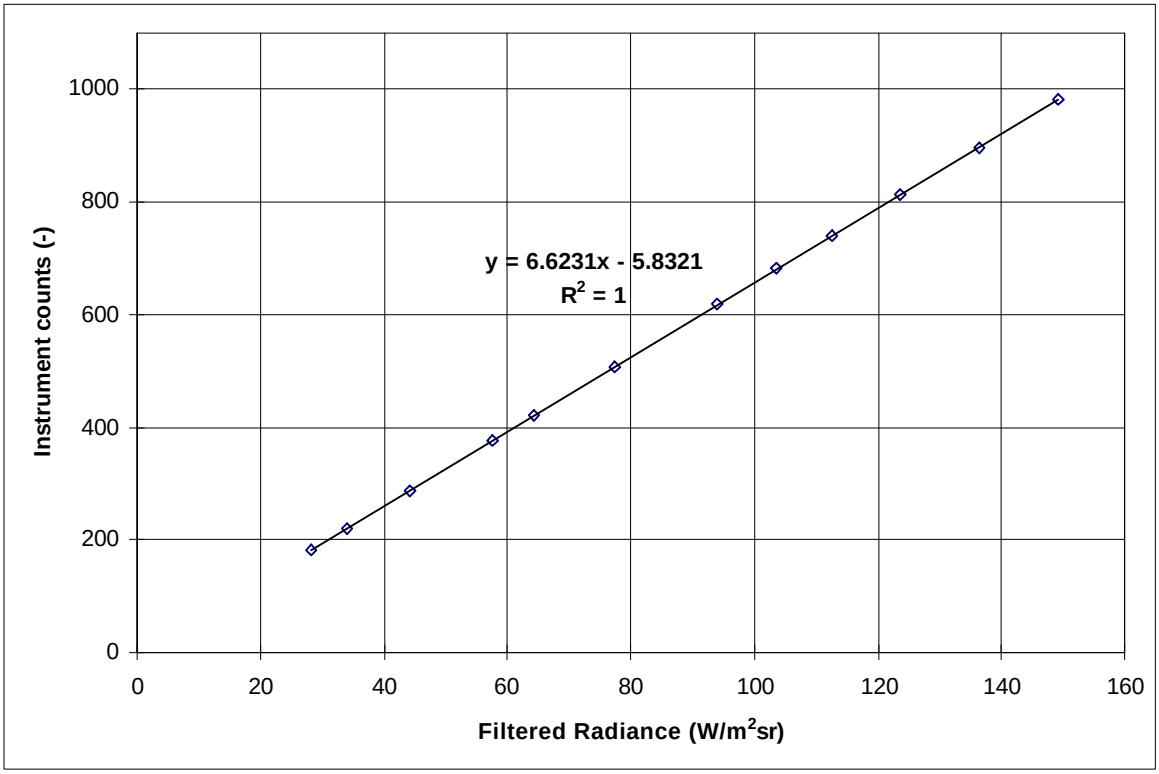

Figure 5.7 Calculation of A_V^{-1} based on the radiometric ground calibration for the PFM total channel sensor.

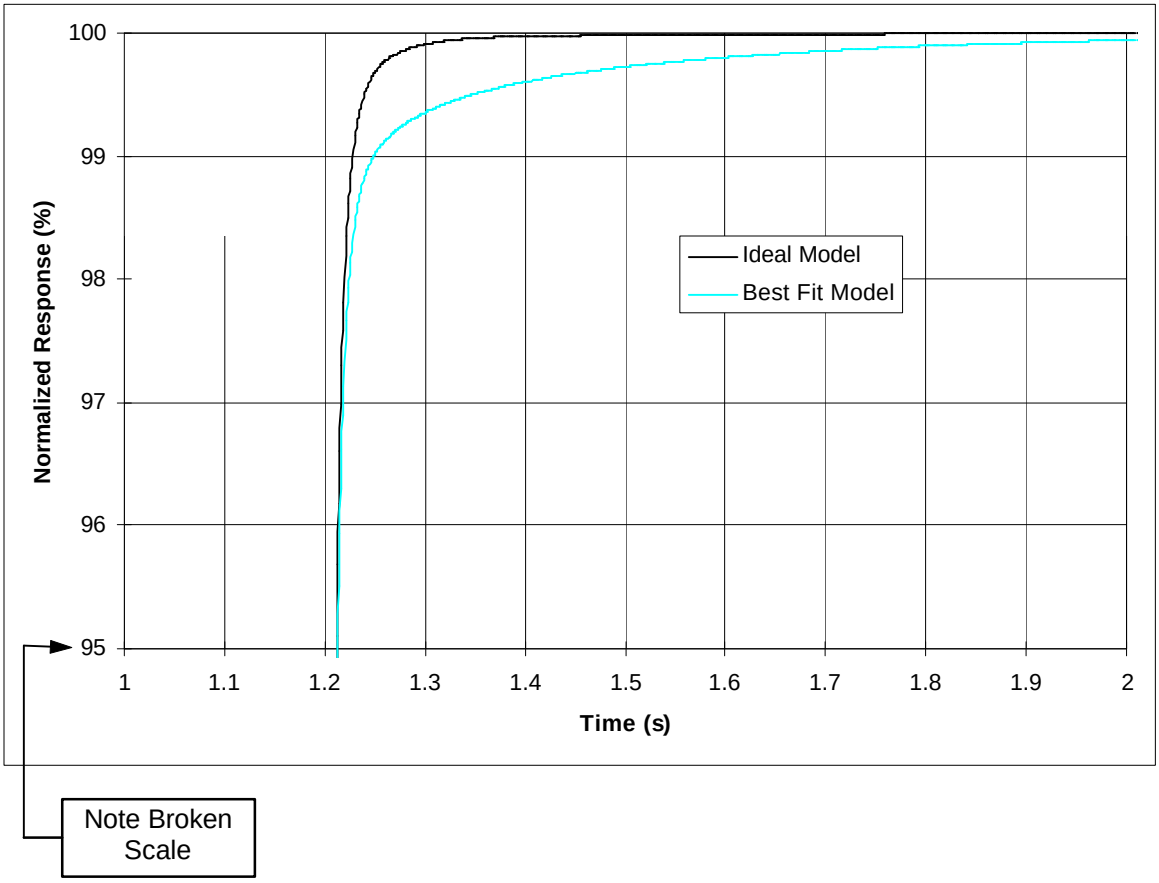

Figure 5.8 Comparison of the ideal model normalized response function with the response function from the “best fit” model version.

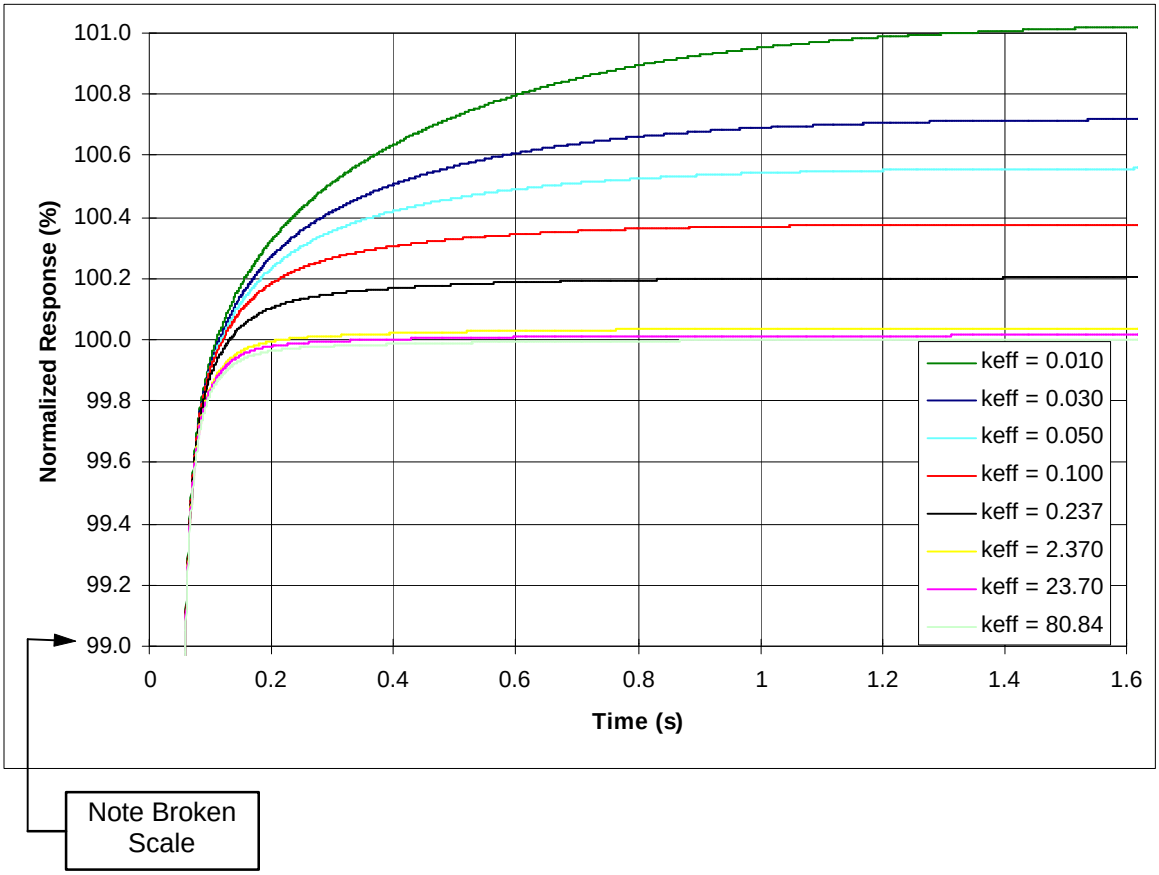

Figure 5.9 Effective increase in responsivity due to varying the value of thermal conductivity, k ($Wm^{-1}K^{-1}$), for the Indium interface.

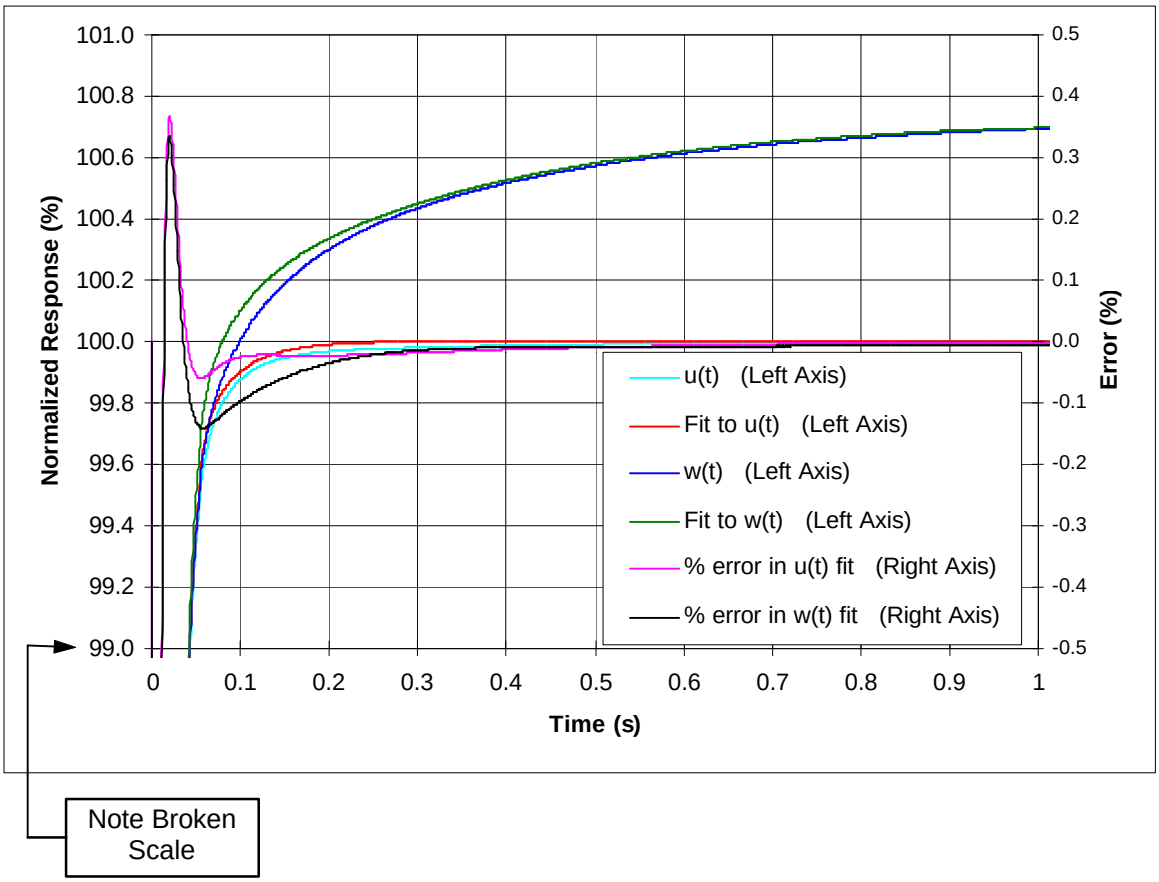

Figure 5.10 Curve fits to the ideal detector response, u(t), and the predicted as-built detector response, w(t).

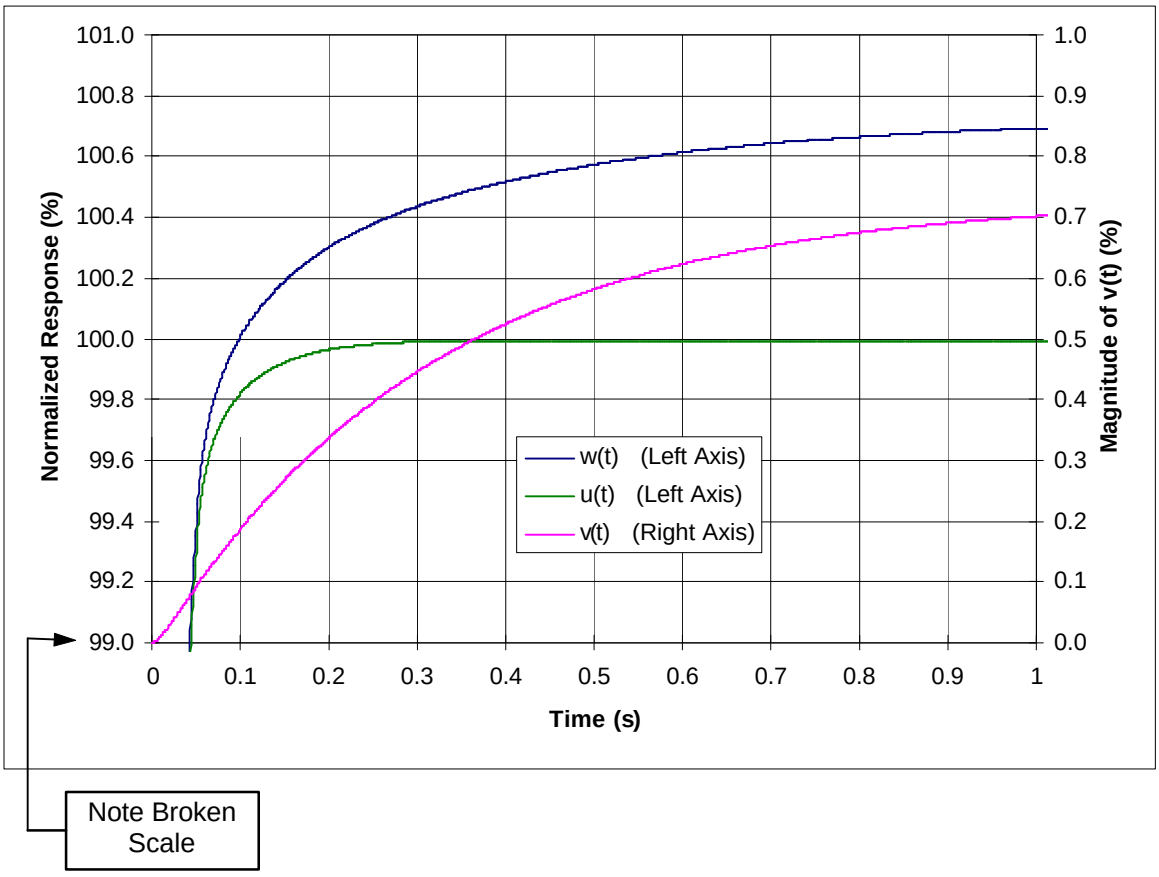

Figure 5.11 Validation of the slow-mode numerical filtering algorithm for a step input at time, t=0.

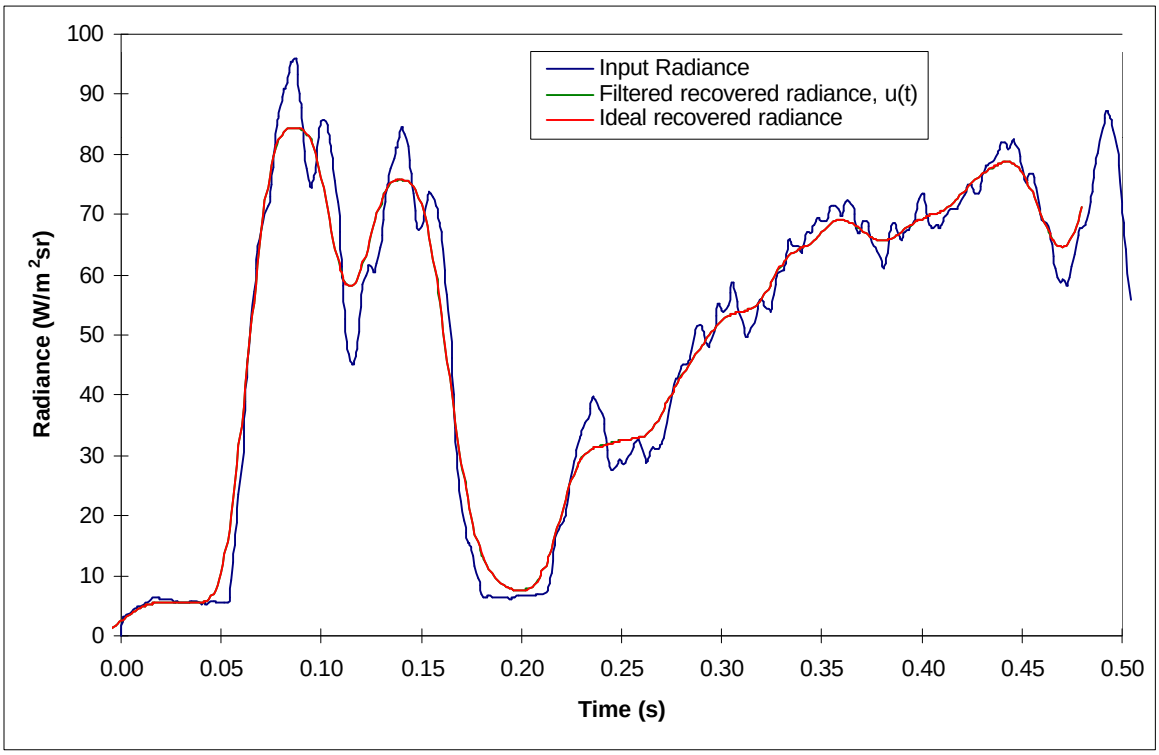

Figure 5.12 Validation of the slow mode filtering algorithm for a nominal Earth scene.

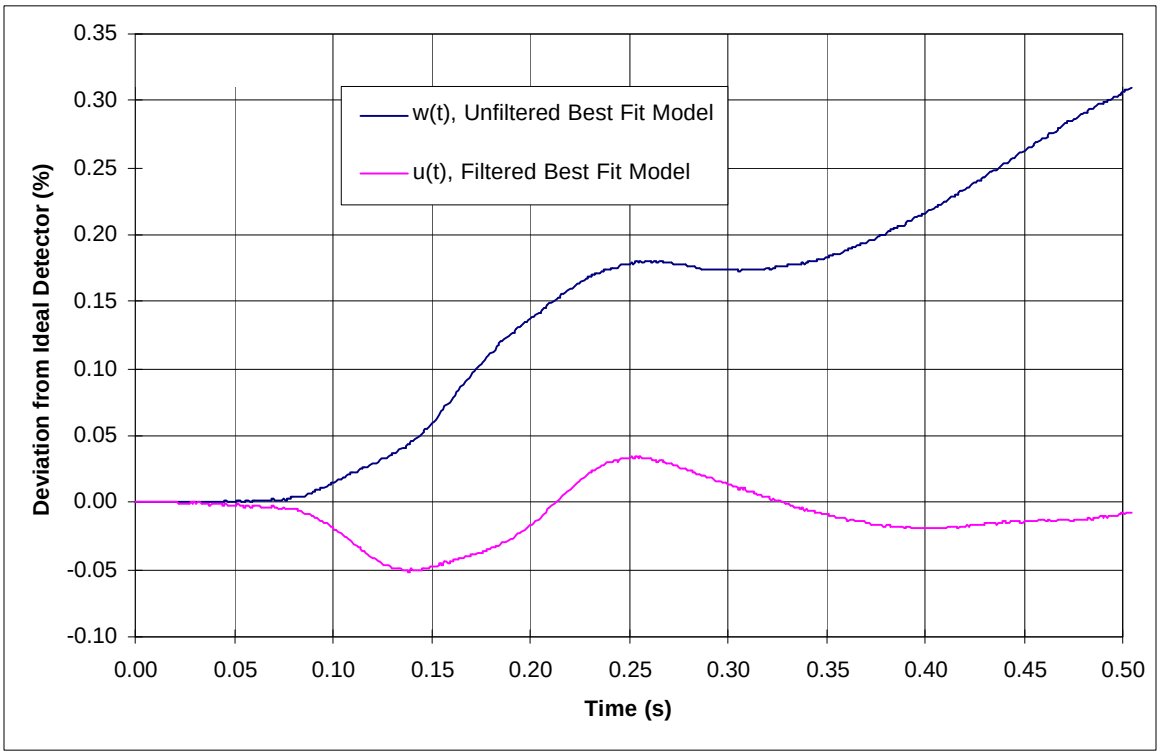

Figure 5.13 Effectiveness of slow-mode numerical filter in forcing the "best fit" model to respond in the same fashion as the ideal model for the radiative input displayed in Figure 5.12.